Ionization from Rydberg atoms and wave packets by scaled terahertz single-cycle pulses

Xiao Wang[1] and F. Robicheaux[1,2,*]

[1]*Department of Physics and Astronomy, Purdue University, West Lafayette, Indiana 47907, USA*
[2]*Purdue Quantum Center, Purdue University, West Lafayette, Indiana 47907, USA*

The strong-field ionization behavior when a Rydberg atom is exposed to a terahertz single-cycle pulse is studied. Fully three-dimensional time-dependent Schrödinger equations and classical trajectory Monte Carlo calculations are performed. Results from stationary eigenstates and Rydberg wave packets are presented, and it is found that the ionization properties can be different for the two cases. All of the pulse parameters and physical quantities are scaled versus the principal quantum number n. The ionized electron's scaled radial, energy, and angular distributions are investigated for different n, and the quantum results are interpreted using a semiclassical method. The scaling relations of quantum interference amplitudes are discussed.

I. INTRODUCTION

Strong-field ionization is a tool commonly used to study and probe atomic and molecular structure. In contrast to deeply bound electrons, Rydberg electrons have many novel properties, such as weak binding energy, high density of states, long period, large dipole moment, etc. The similar frequencies between terahertz radiation and Rydberg orbits makes terahertz field pulses an alternative tool to study the properties of Rydberg electrons.

Strong terahertz radiation was used in many experiments studying field ionization [1–7]. However, strong terahertz single-cycle pulses have only become widely used in the past few years. Strong terahertz single-cycle pulses are usually generated by optical rectification in nonlinear crystals [8,9]. In most cases, the single-cycle pulses are nonsymmetric in the time domain. The effects of asymmetry in field ionization was studied theoretically in Ref. [10,11]. The field strength of terahertz single-cycle pulses can be up to 1 MV/cm [12]. A 1-ps duration is approximately the same as the Rydberg period with principal quantum number $n \sim 20$, which makes the terahertz single-cycle pulse an effective tool to probe and study the periodic motion of Rydberg electrons.

Time-resolved studies of the spatial distributions of Rydberg wave packets have been conducted extensively. Many different optical tools have been used, such as ultraviolet laser pulses [13–15], half-cycle pulses [16–18], single-cycle pulses [19,20], microwaves [21–23], and others. Compared with the other methods, the ionization properties of single-cycle pulses on Rydberg wave packets have not been widely studied. When a single-cycle pulse duration is much shorter than a Rydberg period, previous studies showed that the threshold field amplitude for ionization from a stationary Rydberg state is proportional to $(n/t_w)^2$ [10,11], where n is the principal quantum number and t_w is proportional to the pulse duration. The ionization mechanism is described as displacement ionization. In the present paper, ionization of Rydberg wave packets using single-cycle pulses with durations shorter than or equal to one Rydberg period is studied.

For field pulse ionization due to a long pulse, the scaling relations of ionization thresholds versus the principal quantum number n have been studied before. Different ionization thresholds can be found in different ionization regimes [24]. For ionization due to a single-cycle pulse, only a few studies have been conducted, including experimental [1] and theoretical studies [10,11,25,26]. These studies focused on the ionization probability versus initial pulse parameters or the initial state nl of the Rydberg electron. The distributions and scaling relations of a single variable physical quantity, such as ionization probability, ionized electron angular distribution, energy distribution, etc., are presented in several previous studies [1,11]. There have been no studies on the scaling relations for correlated two-dimensional distributions from single-cycle pulse ionizations in Rydberg atoms. It is well known that classical calculations scale perfectly for different n, but quantum calculations do not scale due to the restrictions from the uncertainty principle. In this paper, comparisons between quantum and classical calculations are studied, including correlated distributions for two physical quantities, at different scaled n states and scaled pulse parameters. Additionally, scaled ionization results for Rydberg wave packets due to a single-cycle pulse are first discussed in this paper.

This paper is structured as follows. Section II gives a brief introduction to the quantum and classical methods used in our calculations. Section III introduces the scaling relations for pulse parameters and all physical quantities. The quantum and classical results in different conditions are compared. Also, the scaled properties of ionization and quantum interference are studied. Section IV introduces the type of Rydberg wave packets used in this paper, and the scaled ionization properties from short- and medium-duration single-cycle pulses are investigated. Atomic units are used throughout the paper unless specified otherwise.

* robichf@purdue.edu

II. METHODS

A. Quantum methods

With a linearly polarized laser pulse in the dipole approximation, a hydrogenic atomic system follows the time-dependent Schrödinger equation:

$$i\frac{\partial \psi}{\partial t} = \left(-\frac{1}{2}\nabla^2 - \frac{1}{r} + F(t)\cdot z \right)\psi, \tag{1}$$

where $F(t)$ is the time-dependent strength of the electric field. The full three-dimensional wave function is expanded on a spherical harmonic basis:

$$\psi(r,\theta,\phi,t) = \sum_{l=0}^{l_{\max}} \frac{R_l(r,t)}{r} Y_{l0}(\theta,\phi). \tag{2}$$

The Y_{lm} are spherical harmonics, and the cylindrical symmetry of $m=0$ is assumed in the present work. The $l_{\max}$ value is the number of angular channels needed to converge all of the physical quantities in the calculations. The radial wave functions can be propagated using various methods. Split operator and Crank-Nicolson methods are used in our calculations. For the radial wave functions, the square-root mesh with a Numerov approximation is adopted. Further details on the wave-function propagation can be found in Ref. [27].

For the single-cycle laser pulse, two different forms are used in our calculations. The first form was introduced in Ref. [26]. It is used in this paper to reinterpret some results from Ref. [26]. The pulse is expressed as

$$F(t) = \begin{cases} -F_m \sin(\omega t), & \text{if } -T < t < 0 \\ -F_m \beta \sin(\beta \omega t), & \text{if } 0 < t < T/\beta \\ 0, & \text{otherwise.} \end{cases} \tag{3}$$

F_m is the peak intensity, and T is the duration of the first half cycle, $T = \pi/\omega$, and β is a factor representing the asymmetry of the pulse. In the calculations, the pulse starts at $t_i = -T$ and ends at $t_f = T/\beta$.

The second form was used in Ref. [10], which is a symmetric, Gaussian-like, single-cycle pulse. It is expressed as

$$F(t) = -C_0 F_m \left(\frac{t}{t_w}\right) \exp\left[-\left(\frac{t}{t_w}\right)^2 - 0.1\left(\frac{t}{t_w}\right)^4 \right], \tag{4}$$

where $C_0 = \sqrt{(\sqrt{35}+5)/5}\,\exp[(\sqrt{35}-4)/4] \approx 2.385$ is a constant that makes the maximum field amplitude to be F_m [10]. The fourth-power term in the exponent is used to shorten the Gaussian tail of the electric field without significantly affecting the properties of a single-cycle pulse. The t_w is a scale of time width of the laser pulse. The electronic wave function is propagated from $t_i = -3.5\,t_w$ to $t_f = +3.5\,t_w$, which gives well-converged results. The second form of the Gaussian-like single-cycle pulse is mainly used in the rest of the paper, due to its smooth expression and no discontinuities in the time domain. Although this paper is based on these two specific pulse types, the results can be generalized to other pulses with similar asymmetry, duration, and strength.

The energy and angular distributions of the ionized electrons are the focus of this paper. At the final time of the calculations, the continuum part of the wave function is expanded using energy-normalized Coulomb eigenstates. The probability amplitude at a positive energy ϵ and angular momentum l can be calculated as

$$a_{\epsilon l} = \int dr\, R_l(r, t=t_f)\, f_{\epsilon l}(r), \tag{5}$$

where $f_{\epsilon l}$ is the energy-normalized regular Coulomb wave function [28]. The energy distributions for ionized electrons can be calculated as

$$\frac{dP}{d\epsilon} = \sum_{l=0}^{l_{\max}} |a_{\epsilon l}|^2. \tag{6}$$

The angular distribution for the ionized part of the electron wave functions at a given energy can be calculated as

$$\frac{d^2 P}{d\cos\theta\, d\epsilon} = 2\pi \left| \sum_{l=0}^{l_{\max}} a_{\epsilon l}\, e^{i\sigma_l}\, Y_{l0}(\cos\theta) \right|^2, \tag{7}$$

where σ_l is the Coulomb phase shift [28]. Note that the cylindrical symmetry of $m=0$ is assumed in our calculations. The integration of Eq. (7) at all positive energies gives the full angular distributions at infinity. The emission angle θ is the polar angle from the field polarization axis.

The radial distributions and the emission angle, just after the pulse is turned off, are also studied in this paper. They are mainly used to compare the results from quantum and classical calculations. The radial distribution of ionized electrons at a given emission angle can be calculated as

$$\frac{d^2 P}{d\cos\theta\, dr} = 2\pi \left| \sum_{l=0}^{l_{\max}} \int d\epsilon\, a_{\epsilon l}\, f_{\epsilon l}(r)\, Y_{l0}(\cos\theta) \right|^2, \tag{8}$$

and the radial distribution averaged over all angles is calculated as

$$\frac{dP}{dr} = \sum_{l=0}^{l_{\max}} \left| \int d\epsilon\, a_{\epsilon l}\, f_{\epsilon l}(r) \right|^2. \tag{9}$$

B. Classical methods

For the strong-field ionization problem, the classical trajectory Monte Carlo method is used [10]. Specifically, consider a quantum problem starting from a stationary Rydberg eigenstate at $|nl\rangle$. By using the microcanonical ensemble treatment [29], the initial energies and angular momenta of the electrons in classical calculations are set to be $E_{\rm cl} = -0.5/n_{\rm cl}^2$, where

$$\left[(n-1)\left(n-\tfrac{1}{2}\right)n\right]^{1/3} < n_{\rm cl} \leqslant \left[n\left(n+\tfrac{1}{2}\right)(n+1)\right]^{1/3},$$
$$\text{and } l^2 - \tfrac{1}{4} < l_{\rm cl}^2 \leqslant (l+1)^2 - \tfrac{1}{4}, \text{ when } l \neq 0, n. \tag{10}$$

For $l=0$ or n, the simple lower or upper bound at 0 or n is used. At a large n and nonzero l, the above two inequalities go to the following approximations:

$$n - 0.5 < n_{\rm cl} \leqslant n + 0.5, \tag{11}$$

$$l < l_{\rm cl} \leqslant l + 1, \tag{12}$$

where the classical quantities $n_{\rm cl}$, $l_{\rm cl}^2$ are uniformly distributed in the given ranges, not the classical energy $-1/2n_{\rm cl}^2$. Comparing with $n_{\rm cl}$ being a single value fixed at n, this

microcanonical ensemble treatment gives better agreement between quantum and classical calculations in some critical cases, which will be shown in Sec. III B.

In order to simulate the radial distribution from a stationary quantum state, all the trajectories start the classical propagations from their respective classical outer turning point at a random time $t_{\mathrm{init}} = t_{\mathrm{turn-on}} - \alpha T_{\mathrm{Ryd}}$ [10]. Here, $t_{\mathrm{turn-on}}$ is the turn-on time of the single-cycle pulse. For example, $t_{\mathrm{turn-on}} = -T$ for a single-cycle pulse in Eq. (3), and $t_{\mathrm{turn-on}} = -3.5 t_w$ for a single-cycle pulse in Eq. (4). α is a uniformly distributed random number between 0 and 1 to simulate the initial radial distribution from a full Rydberg period. The initial angular distribution of the electrons at t_{init} follows $|Y_{l0}(\cos\theta)|^2$. Initial velocity direction of the electron is randomly selected as long as it is perpendicular to the position vector, and the magnitude of velocity is chosen to satisfy the initial angular momentum l_{cl} from the microcanonical ensemble in Eq. (12). The initial direction of the velocity vector can be randomly chosen on the tangential plane because the ionization probability does not depend strongly on this velocity direction from our numerical calculations. Then the electron is propagated considering only the pure Coulomb potential $1/r$ until $t_{\mathrm{turn-on}}$, when the single-cycle pulse electric field turns on. Next the electron trajectory is calculated from both the $1/r$ potential and the single-cycle pulse potential until the pulse turn-off time. To achieve the final angular distribution, the electrons are then propagated to a long fixed final time t_f, when its momentum direction is nearly converged. The statistics of the electrons' final energy and final velocity angle then give classical distributions which are comparable with those from quantum calculations.

Additionally, the classical trajectory Monte Carlo method can be extended to a semiclassical version, which is known as the quantum trajectory Monte Carlo [30]. In this method, the actions along the classical trajectories are calculated. If there is more than one classical path that can go into the same final region, e.g., position or momentum, the amplitudes of the paths are added coherently using the classical actions as the phase factor. The initial electronic states in our calculations are Rydberg states in their position representations. If the final state is in the momentum representation, e.g., when energy versus angle distribution is studied, an extra factor of $-\boldsymbol{p}_f \cdot \boldsymbol{r}_f$ needs to be added to the phase [30]. This is due to the Fourier transform of the wave function to another representation.

III. SCALING RELATIONS

In this section, the scaling behavior of single-cycle pulse ionization with respect to the principal quantum n is studied: we show quantum and classical results for different n but with the field parameters scaled. Specifically, the physical quantities are scaled as follows:

$$r \propto n^2, \; t \propto n^3, \; p\,(\text{momentum}) \propto n^{-1},$$
$$E\,(\text{energy}) \propto n^{-2}, \; F_m \propto n^{-4}, \tag{13}$$

and other unitless quantities are not scaled, such as angle or ionization probability. The nuclear and electronic charges are not scaled. For example, if $F_m = 500$ kV/cm is used at $n = 15$, then the scaled field strength at $n = 30$ can be calculated as 500 kV/cm $\cdot (30/15)^{-4} = 31.25$ kV/cm. It is noted that, due
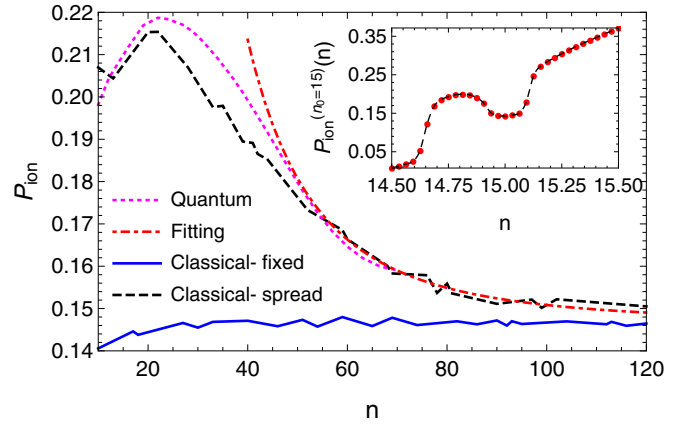

FIG. 1. Ionization probabilities from scaled classical and quantum calculations. The black dashed line is for classical calculations with an initial energy spread of n_{cl} given in Eq. (11). The blue solid line is for classical calculations at a single value of n, and the ionization probability converges to 14.6%. The magenta dotted line is for quantum calculations up to $n = 70$. The red thick line is a fitting for classical results with n_{cl} spread. For $n_{\mathrm{cl}} \geqslant 60$, the fitting function is $P_{\mathrm{ion}} = 0.146 + 4573/n^{3.02}$. The inset figure gives the classical ionization probability when the pulse parameters are fixed at $n_0 = 15$ and the initial classical energy state is at a single value around $n_{\mathrm{cl}} = 15$, see Eq. (14). Scaling relations are given in Eq. (13). Pulse parameters can be found in the text. The initial angular momentum is fixed at $l = 2$.

to the same scaling relations for pulse duration and Rydberg period, durations of the scaled single-cycle pulses will always be the same fraction of one Rydberg period at different n.

As mentioned in Sec. II B, initial energies in classical calculations can either be a single value or be a spread using the microcanonical ensemble treatment. The initial spread in angular momentum l only weakly affects the ionization probability and it is not scaled versus n (see Sec. III A). With all these scaling rules, scaled results from classical calculations at different n, as a single value without spread, should be exactly the same. This is because the classical mechanics of the Coulomb interaction are fully scalable. Conversely, as given in Eq. (11), the microcanonical ensemble treatment requires an energy spread of $\Delta n_{\mathrm{cl}} = 1$, which do not scale with n. This makes the classical calculations using a microcanonical ensemble nonscalable. In quantum calculations, due to the uncertainty principle $\delta x\,\delta p \geqslant 1/2$, results at different n are also different. According to the correspondence principle, the quantum and classical calculations should give the same results as n goes to infinity. For the following part of this section, scaled quantum and classical calculations with different n are performed, and the differences between them are compared.

In Secs. III A and III B, the single-cycle pulse in Eq. (3) is used. In Sec. III C, the single-cycle pulse in Eq. (4) is used.

A. Ionization probabilities versus n

For example, scaled quantum and classical calculations at different n are performed, and the ionization probabilities versus n are shown in Fig. 1. In the calculations, the single-cycle pulse with the form in Eq. (3) is used. At $n = 15$, the pulse

parameters are $F_m = 2.05 \times 10^{-6}$ a.u. $= 10.5$ kV/cm, $T = 1.2402 \times 10^5$ a.u., and $\beta = 1.5$. All parameters are the same as those in Ref. [26] (with a small modification [31]). At other n, the pulse parameters are scaled using relations given in Eq. (13). The initial state always has angular momentum $l = 2$ and is not scaled with n (see next paragraph). Classical results with microcanonical ensemble treatment have much better agreement with quantum results than the classical results with a single value of n. Further details on why a spread of initial energy behaves better than a fixed energy are discussed in the next section.

A very important question related to perfect scaling is how the initial angular momentum l_{cl} should scale and how large the difference is with respect to scaling. l_{cl} determines both the initial angular distribution and the angular momentum of the electron. The angular distribution is a unitless function with respect to angle θ and ϕ, and is not scaled with n. The angular momentum is equal to $v_{init} r_{outer}$ and is scaled proportionally versus n. However, l is a discrete value and cannot be arbitrarily scaled in experiments. To check the differences in ionization probabilities with nonscaled angular momenta, several classical calculations are performed with the only difference being the angular momentum distribution. At a single value of $n = 15$ and identical remaining parameters, the initial angular distributions are kept unchanged as Y_{20}. The initial angular momenta are 0, 1, and 2. Ionization probabilities from these calculations differ by less than 0.5% in the absolute value. Note that, as presented in the blue solid curve of Fig. 1, $l = 2$ at $n = 15$ gives an ionization probability of around 14.5%. In these cases, with the perfect scaling of classical dynamics, ionization probabilities, with $(n, l) = (30, 2) \rightarrow (15, 1)$, $(n, l) = (60, 2) \rightarrow (15, 0.5)$, $(n, l) = (120, 2) \rightarrow (15, 0.25)$, etc., would differ only by less than 0.5%. It can be seen in Fig. 1 that the blue solid curve is mostly flat at large n but with small variations at n near 15. It is shown that, with a nonscaled l_{cl} value, the classical calculations with a single value of n are mostly scalable with small differences at small n.

It is seen in Fig. 1 that the differences between classical calculations using the microcanonical ensemble and a single value of n get smaller as n gets larger. To understand how the two types of calculations converge to the same value as $n \rightarrow \infty$, consider a classical calculation on single-cycle pulse ionization. Let $P_{ion}^{(n_0)}(n)$ be the ionization probability when the principal quantum number is a variable of n and the pulse parameters are scaled for n_0. Then the averaged ionization probability with n being a spread of $n_0 - \delta n$ to $n_0 + \delta n$ can be calculated as

$$\bar{P}(n_0, \delta n) = \frac{1}{2\delta n} \int_{n_0 - \delta n}^{n_0 + \delta n} P_{ion}^{(n_0)}(n) \, dn$$

$$\approx \frac{1}{2\delta n} \int_{n_0 - \delta n}^{n_0 + \delta n} \left[P_{ion}^{(n_0)}(n_0) + P_{ion}'^{(n_0)}(n_0)(n - n_0) \right.$$

$$\left. + \frac{1}{2} P_{ion}''^{(n_0)}(n_0)(n - n_0)^2 + O(n^3) \right] dn$$

$$= P_{ion}^{(n_0)}(n_0) + \frac{1}{6} P_{ion}''^{(n_0)}(n_0)(\delta n)^2. \tag{14}$$

Since classical calculations are perfectly scaled, e.g., $P_{ion}^{(n_0)}(n) = P_{ion}^{(2n_0)}(2n)$, the derivatives can be calculated as

$$P_{ion}^{(n_0)}(n_0 + \delta n) = P_{ion}^{(2n_0)}(2n_0 + 2\delta n),$$

$$\frac{P_{ion}^{(n_0)}(n_0 + \delta n) - P_{ion}^{(n_0)}(n_0)}{\delta n} = \frac{P_{ion}^{(2n_0)}(2n_0 + 2\delta n) - P_{ion}^{(2n_0)}(2n_0)}{\delta n},$$

$$P_{ion}'^{(n_0)}(n_0) = 2 P_{ion}'^{(2n_0)}(2n_0). \tag{15}$$

Thus, the first-order derivative $P_{ion}'^{(n_0)}$ scales as n_0^{-1} and the second-order derivative scales as n_0^{-2}. The average ionization probability from a spread of initial energy at 29.5–30.5 is the same as that of 14.75–15.25. With $\delta n = 0.5$, the series expansion gives n_0^{-2} asymptotic relations for the ionization probability. Also, as $n_0 \rightarrow \infty$, all derivatives go to zero, and the average ionization probability $\bar{P}(n_0, \delta n)$ converges to the single value of $P_{ion}^{(n_0)}(n_0)$.

However, as can be seen in Fig. 1, the ionization probability from classical calculations with n_{cl} being a spread converge as n^{-3} asymptotically to the classical calculations with a single value of n_{cl}. The n^{-3} relation is a coincidence, not a general rule. This is partially due to the fact that the ionization properties at these specific pulse parameters are very sensitive to the initial energy state n of the electron. Since the pulse duration $T_{pulse} = 2.067 \times 10^5$ a.u. is much longer than the Rydberg period at $n = 15$ ($T_{Ryd} = 2.12 \times 10^4$ a.u.), over-the-barrier ionization mechanisms dominate. The maximum field strength $\beta F_m = 3.075 \times 10^{-6}$ a.u. is in the same order as the nuclear Coulomb field strength when the electron is at its outer turning point $[(2 * 15^2)^{-2} = 4.94 \times 10^{-6}$ a.u.$]$. Thus, with pulse parameters fixed at $n_0 = 15$, as n varies from 14.5 to 15.5, the ionization probabilities change rapidly and even nonmonotonically.

As given in the inset of Fig. 1, the ionization probability $P_{ion}^{(15)}(n)$ is very sensitive to the initial classical state n. The average of $P_{ion}^{(15)}(n)$ for n varied from 14.5 to 15.5 gives an ionization probability around 20%, but the $P_{ion}^{(15)}(15)$ itself only gives about 15%. At $n = 15$ and $\delta n > 1/16$, which is equivalent to $n < 120$ and $\delta n = 0.5$, the $P_{ion}^{(15)}(n)$ in Eq. (14) cannot be well expanded as a Taylor series only up to $O(n^3)$. That means the n^{-2} scaling relations derived in Eq. (14) does not hold when n is not large enough. A mixture of n^{-2} and n^{-4} coincidentally gives a scaling relation of n^{-3}, as presented in Fig. 1. It was found that only when n is large enough, e.g., $n > 120$, did the Taylor series expansion in Eq. (14) correctly represent the ionization probability, and a n^{-2} asymptotic relation was found. Further details of ionization properties with n_{cl} from 14.5 to 15.5 are discussed in the next section.

B. Comparisons between quantum and classical methods

Originally found in Ref. [26], as well as shown in Fig. 1 in the previous section, ionization probabilities from a classical calculation at a fixed n of 15 are different from a quantum calculations for $n = 15$. In this section, three calculations are performed to study the ionization probability and physical quantities of this process: fully quantal, classical with n_{cl} fixed at 15, and classical with n_{cl} being a spread from 14.5 to 15.5. The initial angular momentum is set to $l = 2$. The pulse parameters are given in the previous paragraph at $n = 15$.
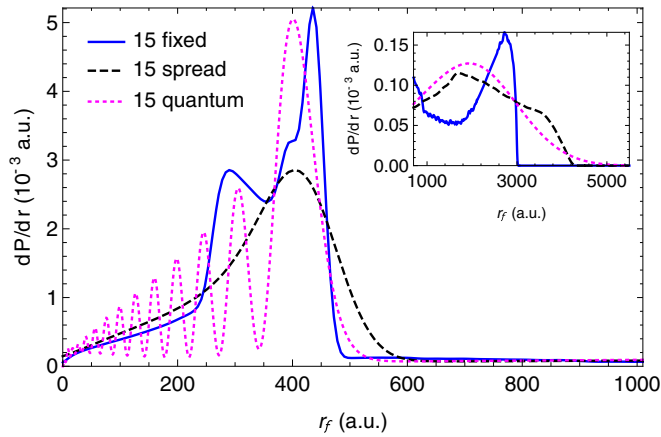
FIG. 2. Full radial distributions at the final time of the pulse, from three different calculations. The initial angular momentum is $l = 2$. The blue solid curve is from a classical calculation with the initial n_{cl} fixed at 15. The black dashed curve is from a classical calculation with the initial n_{cl} being a spread of 14.5–15.5. The magenta dotted curve is from a full quantum calculation starting in a 15d state. The ionization probabilities from the three calculations are 14.3%, 20.7%, and 21.0%, respectively. The inset is a magnification of the distribution with r_f from 700 to 5500 a.u. Note that the probability density scale is different for the inset.
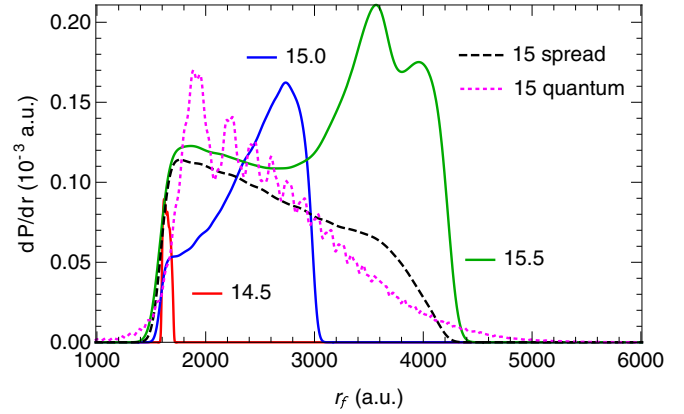

FIG. 3. Radial distributions at the final time of the pulse from classical and quantum calculations. Only those from the ionized part of the distributions are plotted. The red solid curve with small extent around 1600 a.u. is from a classical calculation with n_{cl} fixed at 14.5, and the ionization probability for this case is 0.77%. The green solid curve with the largest extent is from a classical calculation with n_{cl} fixed at 15.5, and the ionization probability for this case is 37.2%. The other three curves are the same calculations as those introduced in the caption of Fig. 2.

The radial distributions at the final time are given in Fig. 2. Both of the classical calculations give overall similar results as compared with the quantum calculation. For the ionized part at around 3000 a.u., results from the classical calculation with n_{cl} fixed at 15 do not match well with the quantum result, while the spread n_{cl} calculation gives much better agreement. As mentioned in the caption of the figure, the ionized wave function is a small portion of the whole wave function. Ionization probabilities and continuum wave functions from the fixed n_{cl} and spread n_{cl} calculations are very different.

To further study the details of the ionized part of the wave function, two more classical calculations for n_{cl} fixed at 14.5 and 15.5 are performed. The continuum radial distributions from quantum and classical calculations are given in Fig. 3. One notable quantity is the ionization probability. For $n_{cl} =$ 14.5, the ionization probability is only 0.77%, but it is 37.2% for $n_{cl} = 15.5$. As shown in the inset of Fig. 1 and discussed in Sec. III A, field ionization processes with these specific field parameters are very sensitive to the initial Rydberg state for this range of n, because the ionization probability and the ionized part of the wave function depend strongly on the initial energy of the Rydberg electron. With that, it is better to use a spread in initial energy, i.e., a microcanonical ensemble treatment, in the classical calculation rather than just a fixed energy as used in Ref. [26].

To verify our applications of the initial energy spread in the classical calculations, the ionized radial and angular distributions at the final time of the pulse are shown in Fig. 4. It can be seen in the figure that the classical calculation with an initial energy spread has a much better agreement with the quantum calculation. Additionally, some interference patterns, with respect to the radial distribution, appear in the quantum results, but not in the classical results. Oscillations

of the quantum interference amplitudes are discussed in the next section.

C. Scaled physical quantities and quantum interferences

Scaled physical quantities from single-cycle pulse ionization with scaled pulse parameters at different n are studied in this section. The single-cycle pulse in Eq. (4) is used in this section, and the pulse parameters are changed to $F_m = 500$ kV/cm, $t_w = 500$ a.u. for $n = 15$ from the previous section. The Rydberg period for the $n = 15$ state is $T_{ryd} = 2\pi n^3 = 21\,206$ a.u. Electrons are initiated in stationary Rydberg eigenstates with angular momentum being zero. Although a single-cycle pulse process with these parameters only gives about 3.8% ionization probability, the small portion of the ionized wave function gives a clear picture for the properties of the ionized electron. The ionization probability is the same for $n = 15$, 30, and 45. As discussed in Sec. III A and in Eq. (14), with the same ionization probability for 15, 30, 45 in quantum calculations, the classical ionization curvature P''_{ion} is negligible in this case. Thus, to mimic the quantum calculation, classical calculations with a single value of n and a single value of l can be performed instead of spreads, and the results would be the same.

The angular distributions for ionized electrons are given in Fig. 5. In the figure, the classical results at different n are scaled and overlapped. However, the results for scaled quantum calculations are different near $\cos \theta_f = 1$. Although not shown in the figure, the rest of the angular distributions for $\cos \theta_f$ from -1 to 0.6 are nearly the same for both quantum and classical, at different n, and they are much smaller than those near $\cos \theta_f = 1$. As can be seen in the figure, as n increases, the quantum angular distributions near $\cos \theta_f = 1$ become sharper. This is very different from the classical results, and the reason for the sharp peak is quantum
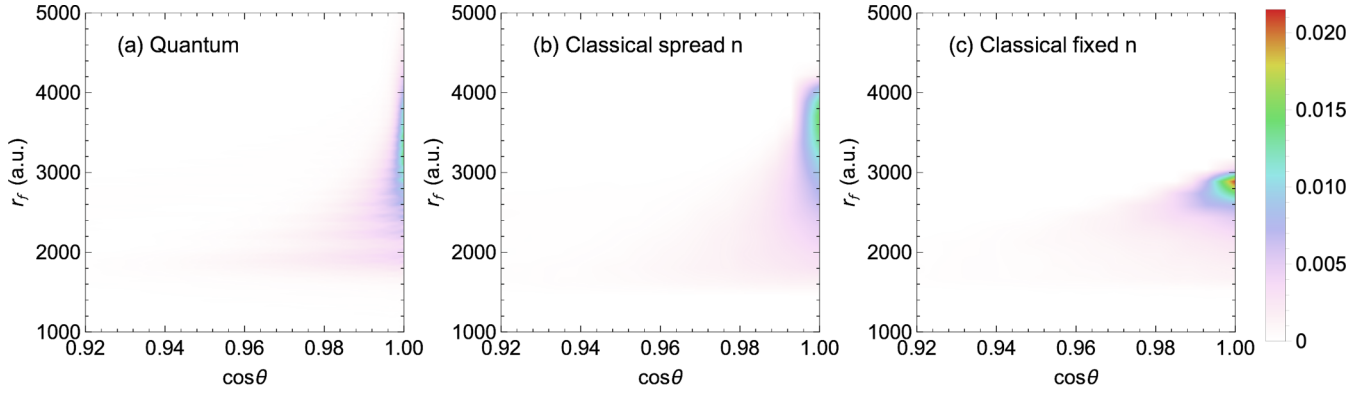
FIG. 4. Correlated distribution of the ionized electron's radial position and its emission angle at the final time of the pulse. Parameters of the field are given in the text of Sec. III A. Figure (a) is from a full quantum calculation, figure (b) is from a classical calculation with n_{cl} being a spread of 14.5–15.5, and figure (c) is from a classical calculation with n_{cl} fixed at 15. The density distributions in all three figures are normalized to their respective ionization probabilities, which can be found in the caption of Fig. 2.

interference. Quantum interference can strengthen distribution at some angles and weaken distribution at other angles.

Using the scaling relations for physical quantities in Eq. (13), the classical action is also scaled, and the scaling is

$$S = \int L \, dt \propto n, \tag{16}$$

where L is the classical Lagrangian. In the present problem, with a small ionization probability, only two classical trajectories can be found that go into the same final angle and same final energy. Actions from the two trajectories scale as n, as well as the difference ΔS between the two trajectories. Since interference maxima can be found at every 2π phase difference, oscillations of interference amplitudes, with respect to scaled physical quantities, would be n times faster at a higher n.

To study the angular distributions in detail, results at scaled final energy slices, $E_f = (15/n)^2 \times 0.002$ a.u., are presented in Fig. 6. In Fig. 6(a), the classical action versus final angle is given. It can be seen that the action differences, ΔS, from the two paths change faster as n gets larger, scaled as the factor of n. In Fig. 6(b), the quantum angular distributions are given. With a larger n, the action varies more rapidly. The amplitudes of angular distributions also oscillate faster. Since the total angular distributions are incoherent summations of angular distributions at all positive energy slices, faster oscillations of the angular distributions away from $\cos\theta_f = 1$ lead to rapid cancellation and flattening of the full angular distribution. With the same ionization probability, constructive summations and sharper peaks around $\cos\theta_f = 1$ can be expected at higher n.

Finally, the correlated distributions of final emission angle and final energy are given in Fig. 7. As mentioned in Sec. III B and Fig. 4, quantum interferences may appear in the correlated distributions at the final time. In Fig. 7, quantum interference with respect to the scaled final energy is found. The differences for classical actions between the two paths are used to determine the quantum interference maxima at E_f. The action differences are aligned at the first
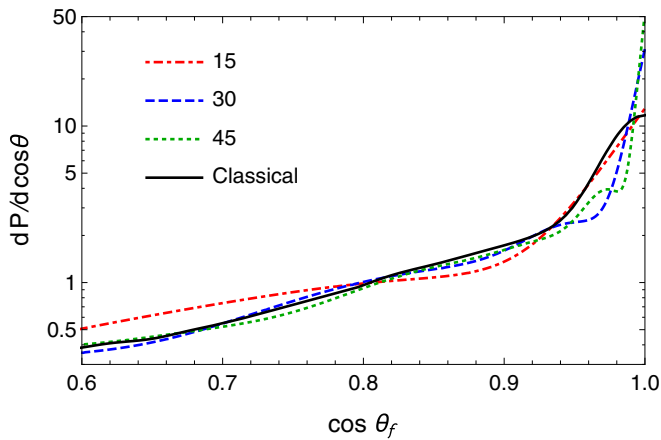

FIG. 5. Angular distributions for ionized electrons from quantum and classical calculations. The initial angular momentum is $l = 0$. Calculations are performed with different n as indicated by the legends and different scaled pulse parameters as indicated in Eq. (13). At $n = 15$, $F_m = 500$ kV/cm and $t_w = 500$ a.u. are used. Classical results at all three n are the same.
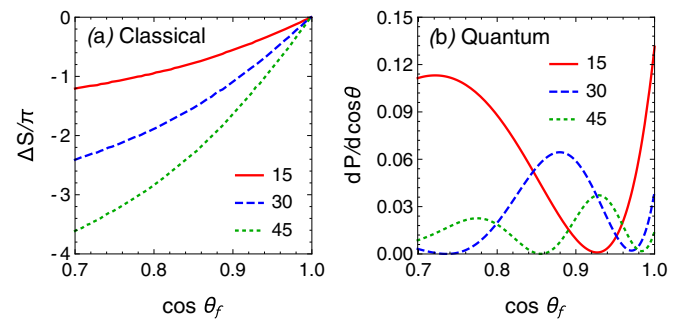

FIG. 6. (a) Classical action differences between two paths vs the final angle, at a scaled final energy. The final energy is scaled for different n, which are $E_f = (15/n)^2 \times 0.002$ a.u. The action differences are aligned as $\Delta S = 0$ at $\cos\theta_f = 1$. (b) Angular distributions at scaled final energies from quantum calculations.
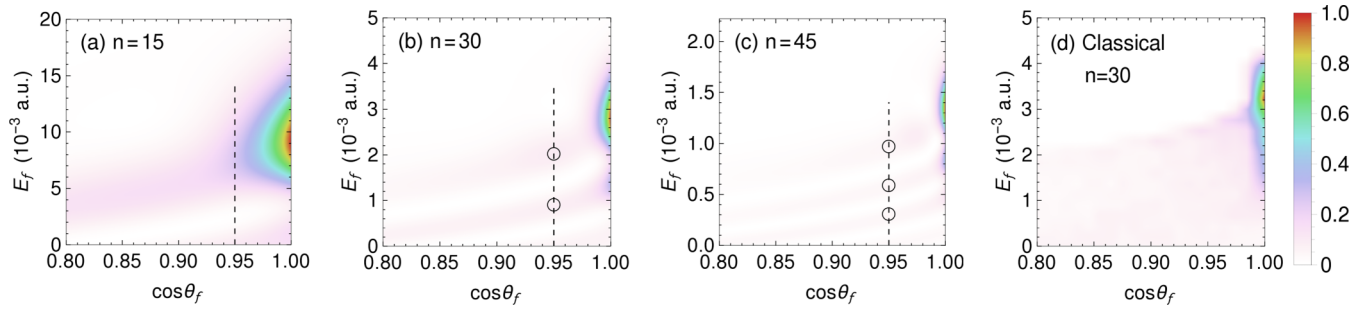
FIG. 7. The correlated energy and angular distributions with scaled pulse parameters at $n = 15$, 30, and 45 for quantum calculations, and at $n = 30$ for classical calculation. The maximum densities are normalized to 1.0 for all figures. The dashed lines are at $\cos\theta_f = 0.95$, while the circles are interference maxima calculated by the semiclassical method introduced in the text.

interference maximum, and all further maxima are found at multiples of 2π phase differences. The classical results are the same for $n = 15$, 30, and 45. No interference is found in the classical results. In the figure of $n = 15$, only one interference maximum can be found in the given range along $\cos\theta_f = 0.95$, while two maxima can be found for $n = 30$ and three for $n = 45$. This interference behavior is due to the fact that semiclassical action is scaled proportional to n while all physical parameters are scaled as those in Eq. (13). Thus, the oscillations of interference amplitudes are also scaled as n versus other scaled parameters. As discussed in Fig. 5, Fig. 6 and earlier in this section, sharper peaks in angular distributions near $\cos\theta_f = 1$ can be found when n is larger. Since the maximum angular momentum scales as n, there are not enough angular channels that can localize the angular distribution near $\cos\theta_f = 1$ at a smaller n.

IV. IONIZATION OF WAVE PACKETS

When dealing with strong-field ionization of Rydberg atoms, the initial state can be either a stationary eigenstate, or a coherent superposition of those eigenstates, which is known as a wave packet. For field ionization with single-cycle pulses, several studies on stationary states have been conducted [1,10,11,25,26]. Since the spatial distribution for stationary states and wave packets can be totally different, the field ionization results are also different for these two scenarios. In this section, the effects of strong-, short-, and medium-duration single-cycle pulses on different initial Rydberg states are studied. The single-cycle pulses with the form of Eq. (4) are used.

Short-duration single-cycle pulses have been studied before [10]. A single-cycle pulse with duration much shorter than one Rydberg period shifts the position of the Rydberg electron by only a small amount without changing its kinetic energy. The small shift in space may introduce a large Coulomb potential energy change if the electron is close to the nucleus. If the electron is far from the nucleus, then the small spacial shift barely changes the Coulomb potential energy. Thus, a short-duration single-cycle pulse provides a tool to probe the spatial distribution of an atomic system. Due to the coherent superposition of the Rydberg wave functions from different energies, the spatial distribution of a Rydberg wave packet changes with time. A short-duration single-cycle

pulse applied at different times yields different ionization probabilities.

Similarly, a medium-duration single-cycle pulse can also be used to probe the spatial distributions of a Rydberg wave packet. In this paper, a medium-duration single-cycle pulse is defined as a single-cycle pulse with its duration approximately the same as one Rydberg period of the Rydberg electron. With a medium-duration single-cycle pulse, the highest ionization probability is achieved when most of the electron distribution is near the nucleus when the single-cycle pulse goes through zero. This can be understood in that an electron reverses velocity at the inner turning point at the same time as the electric field of a single-cycle pulse reverses [20]. Thus, a medium-duration single-cycle pulse provides similar ionization properties as a short-duration single-cycle pulse with respect to the probe of the electron spatial distribution. It is similar to those many-cycle long pulse ionizations on Rydberg wave-packet experiments [13–15], where the Rydberg wave packets absorb energy and become ionized when they are near the nucleus.

The type of Rydberg wave packet used in this paper is the superposition of two adjacent Rydberg eigenstates with a variable relative phase:

$$|\psi(t_i)\rangle = \frac{n^{3/2}|nl\rangle + e^{i\varphi}(n+1)^{3/2}|(n+1)l\rangle}{\sqrt{n^3 + (n+1)^3}}, \qquad (17)$$

where $\varphi = -(E_{n+1} - E_n)t_i + \varphi_0$, t_i is the starting time of the pulse, and φ_0 is a controllable parameter between 0 and 2π, which gives the superposition phase of wave packets at $t = 0$.

The two stationary states in Eq. (17) are not superposed with equal weight. The $n^{3/2}$ factor before the $|nl\rangle$ state is due to the properties of radial wave functions of hydrogenic eigenstates [32]

$$R_n(r) \sim n^{-3/2} f(r) \quad \text{at small radius } r, \qquad (18)$$

where $f(r)$ is a radial function that does not depend on principal quantum number n. This asymptotic behavior at small radius can be used to add up the radial wave functions from $|nl\rangle$ and $|(n+1)l\rangle$ constructively or destructively at small radius. The wave packet in Eq. (17) can thus have most of its radial distributions near the nucleus or far from the nucleus. As an example, radial wave functions of the coherent superpositions of 15s and 16s states are shown in Fig. 8. Experimentally, the $n^{3/2}$ factor can be achieved by fine tuning
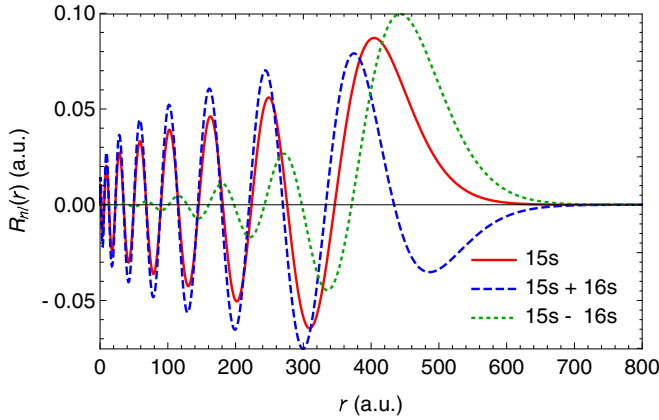
FIG. 8. Radial wave functions of the hydrogen $15s$, "$15s + 16s$," and "$15s - 16s$" states. Note that the $15s$ and $16s$ states do not have the equal weight ($1/\sqrt{2}$) in the superpositions, see Eq. (17). The "$15s + 16s$" represents a wave packet of $\varphi_0 = 0$, while "$15s - 16s$" represents $\varphi_0 = \pi$.

the frequency and width of a laser pulse used to generate the Rydberg wave packet.

Several quantum calculations were performed to study the ionization probabilities versus φ_0, and the results can be found in Fig. 9. In the figure, the ionization probabilities have huge differences at different superposition phases. At $\varphi_0 \approx 0$, the wave packets add constructively at small radius, and the ionization probabilities are at a maximum. At $\varphi_0 \approx \pi$, the wave packets add destructively at small radius. Most of the electron probability is away from the nucleus, and the ionization probabilities are at a minimum. The ionization probabilities satisfy simple cosine relations versus the initial phase, and the fitting functions are given in the figure caption. Also, the φ_0-averaged ionization probabilities are the same as
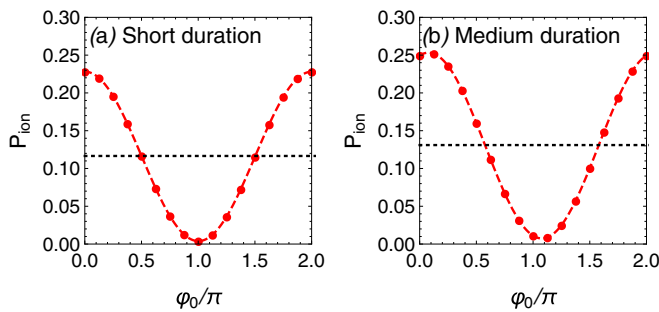

FIG. 9. Ionization probabilities for $15s + \exp(i\varphi_0)16s$ wave packets vs the superposition phase φ_0 as given in Eq. (17). (a) A short-duration pulse process with $F_m = 2000$ kV/cm and $t_w = 606$ a.u. (b) A medium-duration pulse process with $F_m = 60$ kV/cm and $t_w = 3029$ a.u., where the pulse duration is approximately one Rydberg period for $15s$ state: $7.0 t_w = T_{\mathrm{Ryd}} \approx 21\,206$ a.u. The black dotted lines are weighted averages of ionization probabilities for stationary $15s$ and $16s$ states, separately. The averages are 11.7% and 13.1% for the two processes, respectively. The red points are from quantum calculations, while the red dashed lines are their fittings. The fitting functions are $0.116 + 0.112 \cos(\varphi_0 - 0.057)$ and $0.130 + 0.123 \cos(\varphi_0 - 0.245)$ for the two processes, respectively. Details for the fitting functions can be found in the Appendix.
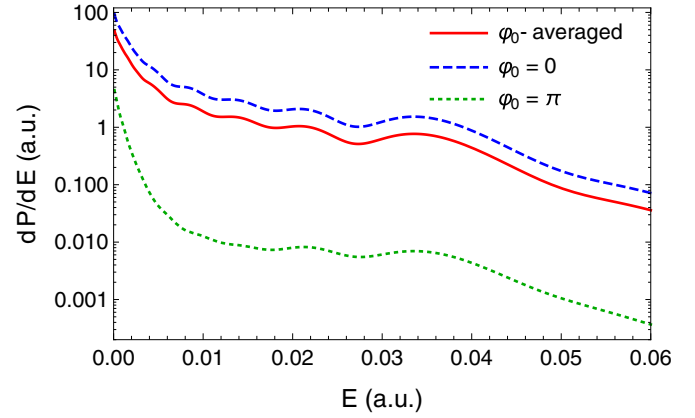

FIG. 10. Energy distributions for ionizations from $15s + \exp(i\varphi_0)16s$ wave packets as introduced in Eq. (17). A short-duration single-cycle pulse with parameters in the caption of Fig. 9(a) is used. The results are plotted for $\varphi_0 = 0$, π, and averages of φ_0 ranging from 0 to 2π.

the weighted average ionization probabilities for $15s$ and $16s$. These properties can be derived from the coherent superposition of the wave packets. Details for the ionization probability versus φ_0 can be found in the Appendix.

As derived in the Appendix, the ionization probability versus superposition phase φ_0 satisfies (assuming initial weights of the two stationary states are approximately the same)

$$P_{\mathrm{ion}} \simeq \bar{P}_{\mathrm{st}} + A\cos(\varphi_0 + \varphi_s), \quad \text{where}$$

$$A e^{i\varphi_s} = \sum_l \int_0^\infty d\epsilon \, \langle \psi_{f1}|\epsilon \, l\rangle\langle \epsilon \, l|\psi_{f2}\rangle. \quad (19)$$

The $\bar{P}_{\mathrm{st}}$ is the φ_0-averaged ionization probability. The $|\psi_{f1}\rangle$ and $|\psi_{f2}\rangle$ are continuum wave functions ionized from the two stationary states in Eq. (17). The maximum ionization probabilities are slightly shifted from zero phase, where the shifts φ_s of 0.057 and 0.245 radians are found. The small phase shift is the argument of the overlap integral of continuum wave functions ionized from the two stationary states. The depth of the ionization curve is determined by the amplitude of the overlap integral. For both short- and medium-duration single-cycle pulse ionizations, the minimum allowed ionization probability is very close to zero. This indicates that $A \simeq \bar{P}_{\mathrm{st}}$, and the overlap integral nearly reaches the maximum. As a comparison, the ionization curve due to a medium-duration single-cycle pulse is slightly deeper than that of a short-duration single-cycle pulse. In this case, the continuum wave functions ionized from two adjacent states due to a medium-duration single-cycle pulse have a slightly larger overlap than those due to a short-duration single-cycle pulse.

Energy distributions of the ionized wave functions from wave packets with different superposition phase φ_0 are given in Fig. 10. In the calculations, short-duration single-cycle pulses are used. Pulse parameters and ionization probabilities can be found in Fig. 9(a). Most of the ionized wave functions are at low energies, and the energy distribution is decreasing versus E. Since the majority of the electron radial distributions from the wave packet of $\varphi_0 = \pi$ are at the

outer turning point, the displacement-caused potential energy change by a short single-cycle pulse is much smaller than that of the $\varphi_0 = 0$ case. Thus, the energy distribution from $\varphi_0 = \pi$ decreases much faster and earlier than that of $\varphi_0 = 0$ and the φ_0-averaged results. Ionization probability from $\varphi_0 = 0$ is at a maximum, while $\varphi_0 = \pi$ is at a minimum. It can be proved that $P_{\text{ion}}(\varphi_0) + P_{\text{ion}}(\varphi_0 + \pi) = 2\bar{P}_{\text{st}}$. It can be seen in the figure that the φ_0-averaged ionization probability is always the average of those from $\varphi_0 = 0$ and π, at all energies.

Additionally, scaling relations for ionizations from Rydberg wave packets are also studied. Instead of the $|15s\rangle + e^{i\varphi_0}|16s\rangle$ state, the initial wave packet is changed to $|30s\rangle + e^{i\varphi_0}|31s\rangle$ and $|45s\rangle + e^{i\varphi_0}|46s\rangle$ states. Using the scaling relations given in Eq. (13), the pulse parameters are scaled versus the principal quantum number n. For all three wave packets given here, although $\Delta n = 1$ is not scaled as n, curves of ionization probabilities versus φ_0 due to both short- and medium-duration pulses are nearly the same as those in Fig. 9. For short- or medium-duration pulses, at $t = 0$, only those electrons within a small radius near the nucleus can be ionized [11]. The critical radius is proportional to the free electron shift in a field pulse, $r_c \propto F_m t_w^2$, and is also scaled as n^2. In all three wave packets $|15s\rangle + e^{i\varphi_0}|16s\rangle$, $|30s\rangle + e^{i\varphi_0}|31s\rangle$, and $|45s\rangle + e^{i\varphi_0}|46s\rangle$, the probabilities to find electrons within a small radius ($r_c < 2n^2$) are nearly the same, since they all have $\Delta n = 1$. Thus, the curves of ionization probability are also the same for all three wave packets, and for both short- and medium-duration pulses.

Classical calculations are performed to investigate the ionization probability versus the radial distributions of wave packets. Electrons are initiated at the energy and angular momentum of a $15s$ state. The pulse parameters for short- and medium-duration pulses are defined in Fig. 9. For every r_{init} at $t = -3.5\,t_w$, two separate classical trajectories are calculated. The first trajectory includes the field pulse and the $1/r$ core Coulomb potential, while the second trajectory considers only the $1/r$ core Coulomb potential. Then the ionization probability from the first trajectory averaged over θ is plotted versus radial position at $t = 0$ from the second trajectory, which is independent of θ. The ionization probability versus r at $t = 0$ can be found in Fig. 11. This figure can be compared with Fig. 8, since φ_0 in Eq. (17) gives the radial distribution of wave packets at $t = 0$ when there is no single-cycle pulse. For example, for the short pulse in Fig. 11, electrons are ionized only when they have $r \lesssim 250$ at $t = 0$. For the medium-duration pulse, electrons can be ionized when they are slightly farther away from the nucleus at $t = 0$, and the ionization probability curve is smoother than that of a short pulse. Additionally, for a wave packet of $15s - 16s$ with $\varphi_0 = \pi$, illustrated as the green dotted line in Fig. 11, the probability to find the electron within $r_c \lesssim 250$ a.u. is very small. The ionization probabilities can be estimated from an integral

$$\tilde{P}_{\text{ion,est}} = \int dr \, |\psi(r)|^2 P_{\text{ion}}(r). \tag{20}$$

For $\varphi_0 = \pi$, the integral gives ionization probabilities of 0.3% for the short-duration pulse and 0.9% for the medium-duration pulse. These values are very close to values at the minima in the quantum calculations in Fig. 9.
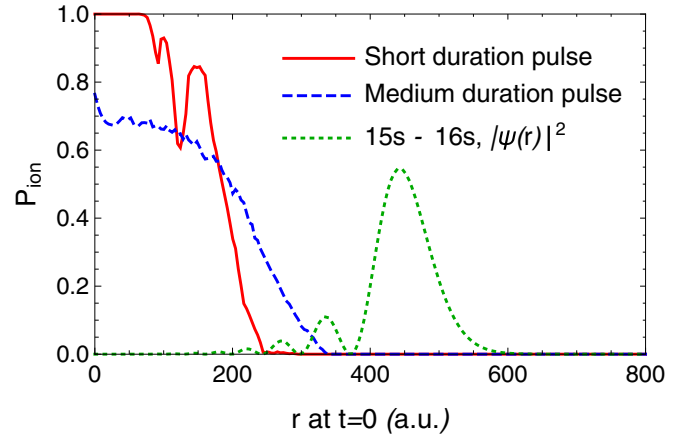

FIG. 11. Ionization probability from classical calculations vs the radial position r of electron at $t = 0$. The electron is initiated at energy of $n = 15$ and angular momentum of zero, where the distance of the classical outer turning point is approximately $2n^2 = 450$ a.u. See text for details of r. Short- and medium-duration pulses are defined in the caption of Fig. 9. The radial distribution from a wave packet of $15s - 16s$ with $\varphi_0 = \pi$, as shown in Fig. 8 and Eq. (17), is plotted as a reference. The radial distribution is plotted in arbitrary units.

The ionization probabilities from Rydberg wave packets at different superposition phases can differ by a factor of 5 or more. A short- or medium-duration single-cycle pulse can be used as highly efficient time-resolved probe to study the spatial distributions of Rydberg wave packets.

V. CONCLUSIONS

In this paper, the scaling behavior for terahertz single-cycle pulse ionization from a Rydberg atom was studied. Two different forms of single-cycle pulses were used in this paper, an asymmetric pulse [26] and a symmetric pulse [10]. A previous study [26] found discrepancies between the quantum and classical calculations for single-cycle pulse ionizations of a Rydberg atom. Results from quantum calculations, classical calculations with a single value of n, and classical calculations using a microcanonical ensemble treatment are compared in detail. In some critical cases of over-the-barrier ionizations where the field strength is near the ionization threshold, classical calculations with a spread of n give much better agreement with the quantum calculations. The scalings for pulse parameters and other physical quantities versus principal quantum number n were studied. With the scaled physical quantities, classical results with a single value of n are nearly perfectly scaled, but the quantum results are not. Interferences in the correlated distributions of the electron's final energy and emission angle were studied by quantum and semiclassical methods. It was found that the oscillations of interference amplitudes scale as n.

Single-cycle pulse ionization from Rydberg wave packets was also studied. The Rydberg wave packets were introduced as a superposition of $|nl\rangle$ and $|(n+1)l\rangle$ states with a different relative superposition phase. The ionization probabilities versus superposition phase were studied for both short- and medium-duration single-cycle pulses, and sinusoidal relations

were found. The amplitude and argument of the overlap integral of ionized wave functions were discussed. The overlap integral determines the depth and shift of the ionization curve. Additionally, ionization with scaled pulses from Rydberg wave packets was also studied. Scaled pulses at higher n wave packets yield nearly the same ionization curves as for lower n, for both short- and medium-duration single-cycle pulse.

ACKNOWLEDGMENTS

APPENDIX: WAVE-PACKET IONIZATION PROBABILITIES VERSUS SUPERPOSITION PHASE φ_0

The initial wave packet before the single-cycle pulse is given in Eq. (17):

$$|\Psi_i\rangle = c_1|n_1 l\rangle + c_2 e^{i\varphi_0}|n_2 l\rangle, \tag{A1}$$

where c_1 and c_2 are real amplitudes for the two states as given in Eq. (17) and φ_0 is the superposition phase of the wave packet. Since the Schrödinger equation is linear, the final wave function after the single-cycle pulse can be written as

$$|\Psi_f\rangle = c_1|\psi_{f1}\rangle + c_2 e^{i\varphi_0}|\psi_{f2}\rangle, \tag{A2}$$

where c_1, c_2, and φ_0 are exactly the same numbers as those in Eq. (A1). Here, $|\psi_{f1}\rangle$ and $|\psi_{f2}\rangle$ are the respective wave functions after single-cycle pulse ionization for the initial stationary states $|n_1 l\rangle$ and $|n_2 l\rangle$. The ionization probability for the wave packet can be calculated as ($|\epsilon\, l\rangle$ is the energy-

normalized continuum eigenstate)

$$
\begin{aligned}
P_{\text{ion}} &= \sum_l \int_0^\infty d\epsilon\, |\langle \epsilon\, l|\Psi_f\rangle|^2 \\
&= \sum_l \int_0^\infty d\epsilon\, |\langle \epsilon\, l|c_1\psi_{f1} + c_2 e^{i\varphi_0}\psi_{f2}\rangle|^2 \\
&= \sum_l \int_0^\infty d\epsilon\, \big[c_1^2|\langle \epsilon\, l|\psi_{f1}\rangle|^2 + c_2^2|\langle \epsilon\, l|\psi_{f2}\rangle|^2 \\
&\quad + c_1 c_2 e^{i\varphi_0}\langle\psi_{f1}|\epsilon\, l\rangle\langle\epsilon\, l|\psi_{f2}\rangle + \text{c.c.}\big]. \tag{A3}
\end{aligned}
$$

Note that integration over the first two terms is the weighted average of ionization probabilities from the two stationary states, defined to be $\bar{P}_{\text{st}}$. Let the continuum wave-function projection be

$$\sum_l \int_0^\infty d\epsilon\, \langle\psi_{f1}|\epsilon\, l\rangle\langle\epsilon\, l|\psi_{f2}\rangle = A e^{i\varphi_s}, \tag{A4}$$

where A is the real amplitude and φ_s is the argument for the projection. The ionization probability in Eq. (A3) can be simplified as

$$P_{\text{ion}} = \bar{P}_{\text{st}} + 2c_1 c_2 A \cos(\varphi_0 + \varphi_s). \tag{A5}$$

This explains that the φ_0-averaged probabilities of P_{ion} are always the same as the weighted averages of the stationary state ionization probabilities. By comparing Eq. (A5) with wave-packet ionization curves in Fig. 9, the projection phase φ_s of the two continuum wave functions can be determined.

For c_1, c_2 from Eq. (17) at a large n, it can be shown that $2c_1 c_2 \simeq 1$. Thus, Eq. (A5) can be simplified as

$$P_{\text{ion}} \simeq \bar{P}_{\text{st}} + A \cos(\varphi_0 + \varphi_s). \tag{A6}$$

The overlap amplitude A of the continuum wave functions, as given in Eq. (A4), significantly affect the depth of ionization probabilities versus φ_0. When $c_1 = c_2 = 1/\sqrt{2}$, $A \leqslant \bar{P}_{\text{st}}$, which gives the upper bound of the overlap integral of the two continuum wave functions.

[1] S. Li and R. R. Jones, Phys. Rev. Lett. **112**, 143006 (2014).

[2] X. Ropagnol, M. Khorasaninejad, M. Raeiszadeh, S. Safavi-Naeini, M. Bouvier, C. Y. Côté, A. Laramée, M. Reid, M. A. Gauthier, and T. Ozaki, Opt. Exp. **24**, 11299 (2016).

[3] H. A. Hafez, X. Chai, A. Ibrahim, S. Mondal, D. Férachou, X. Ropagnol, and T. Ozaki, J. Opt. **18**, 093004 (2016).

[4] S. Li and R. Jones, Nat. Commun. **7**, 13405 (2016).

[5] K. Iwaszczuk, M. Zalkovskij, A. C. Strikwerda, and P. U. Jepsen, Optica **2**, 116 (2015).

[6] G. Herink, L. Wimmer, and C. Ropers, New J. Phys. **16**, 123005 (2014).

[7] L. Wimmer, G. Herink, D. Solli, S. Yalunin, K. Echternkamp, and C. Ropers, Nat. Phys. **10**, 432 (2014).

[8] M. C. Hoffmann and J. A. Fülöp, J. Phys. D: Appl. Phys. **44**, 083001 (2011).

[9] K. Reimann, Rep. Prog. Phys. **70**, 1597 (2007).

[10] B. C. Yang and F. Robicheaux, Phys. Rev. A **91**, 043407 (2015).

[11] B. C. Yang and F. Robicheaux, Phys. Rev. A **90**, 063413 (2014).

[12] H. Hirori, A. Doi, F. Blanchard, and K. Tanaka, Appl. Phys. Lett. **98**, 091106 (2011).

[13] J. A. Yeazell, M. Mallalieu, and C. R. Stroud, Phys. Rev. Lett. **64**, 2007 (1990).

[14] J. A. Yeazell and C. R. Stroud, Phys. Rev. A **43**, 5153 (1991).

[15] J. L. Krause, K. J. Schafer, M. Ben-Nun, and K. R. Wilson, Phys. Rev. Lett. **79**, 4978 (1997).

[16] R. R. Jones, Phys. Rev. Lett. **76**, 3927 (1996).

[17] J. Ahn, D. N. Hutchinson, C. Rangan, and P. H. Bucksbaum, Phys. Rev. Lett. **86**, 1179 (2001).

[18] C. Raman, C. W. S. Conover, C. I. Sukenik, and P. H. Bucksbaum, Phys. Rev. Lett. **76**, 2436 (1996).

[19] T. Zhou, S. Li, and R. R. Jones, Phys. Rev. A **89**, 063413 (2014).

[20] X. Wang and F. Robicheaux, Phys. Rev. A **96**, 043409 (2017).

[21] J. E. Bayfield and P. M. Koch, Phys. Rev. Lett. **33**, 258 (1974).

[22] P. Pillet, W. W. Smith, R. Kachru, N. H. Tran, and T. F. Gallagher, Phys. Rev. Lett. **50**, 1042 (1983).

[23] M. W. Noel, W. M. Griffith, and T. F. Gallagher, Phys. Rev. Lett. **83**, 1747 (1999).

[24] L. Keldysh, Sov. Phys. JETP **20**, 1307 (1965).

[25] H. Agueny, M. Chovancova, J. P. Hansen, and L. Kocbach, J. Phys. B: At. Mol. Opt. **49**, 245002 (2016).

[26] M. Chovancova, H. Agueny, J. J. Rørstad, and J. P. Hansen, Phys. Rev. A **96**, 023423 (2017).

[27] F. Robicheaux, J. Phys. B: At. Mol. Opt. **45**, 135007 (2012).

[28] H. Friedrich, in *Theoretical Atomic Physics*, Graduate Texts in Physics (Springer International Publishing, Cham, Switzerland, 2017).

[29] R. L. Becker and A. D. MacKellar, J. Phys. B: At. Mol. Opt. **17**, 3923 (1984).

[30] N. I. Shvetsov-Shilovski, M. Lein, L. B. Madsen, E. Räsänen, C. Lemell, J. Burgdörfer, D. G. Arbó, and K. Tőkési, Phys. Rev. A **94**, 013415 (2016).

[31] The parameters in the caption of Fig. 5 of Ref. [26] were used, except the field strength. From a private communication (J. P. Hansen), $F_m = 2.05 \times 10^{-6}$ a.u. $= 10.5$ kV/cm instead of 18 kV/cm was used. With that, the same ionization probability of 20% as indicated in their figure caption can be achieved.

[32] M. Aymar, C. H. Greene, and E. Luc-Koenig, Rev. Mod. Phys. **68**, 1015 (1996).